Journal of Volcanology and Geothermal Research 363 (2018) 10–22

Contents lists available at ScienceDirect

Journal of Volcanology and Geothermal Research

journal homepage: www.elsevier.com/locate/jvolgeores

An experimental study of the flow structure and acoustics of jets: Implications for volcano infrasound

Elizabeth Swanson[a,*], Raf Theunissen[a], Alison Rust[a], David Green[b], Jeremy Phillips[a]

[a] University of Bristol, Bristol, UK
[b] AWE Blacknest, Brimpton, Reading, UK

ARTICLE INFO

Article history:
Received 20 February 2018
Received in revised form 14 August 2018
Accepted 17 August 2018
Available online 23 August 2018

Keywords:
Acoustics
Infrasound
Jet noise
PIV
Volcano

ABSTRACT

Aeroacoustic jet noise theory describes the relationship between acoustic signals and jet operating parameters. Based on empirical aeroacoustic relationships, a link between peak frequency and amplitude and jet diameter and velocity has been used by volcano acousticians to return the operating parameters of column generating volcanic eruptions. There are however significant differences between the nozzle geometries and structures of flows studied in the aeroacoustic literature and flows emitted from volcanic vents. These differences raise questions as to the validity of applying engineering relationships to volcanic eruptions. Combining particle image velocimetry and acoustic data we investigated the flow structures, acoustic signals and dominant source locations of jet flows emitted from three simple nozzle geometries (convergent, straight and divergent). Flows from the straight and divergent nozzles exited in a more developed flow regime than those emitted from convergent nozzles. While for the convergent nozzles dominant sound sources were located within the jet flow, the dominant signals from the straight and divergent nozzles were located in the region of the nozzle exit. Consequently, for the straight and divergent nozzles it was not possible to differentiate between signals generated by the jet flow and those generated by internal sound sources without beamforming analysis. In order to better replicate the volcanic case and in contrast to studies for industrial applications, our experimental test section was not engineered to minimise internal noise. Without acoustic treatment such as screens, choke plates and paddles, jet noise signals were contaminated by signals generated within the test rig and so, even for the convergent nozzles, the aeroacoustic relationships derived from engineering studies could not be used to retrieve the jet operating parameters. Our results indicate that in the volcanic case, the raw acoustic spectra will contain signals generated by both in-conduit and above-vent processes. Therefore inversions for volcanic jet parameters such as mass eruption rate from standard aeroacoustic relationships may be unreliable.

1. Introduction

Developments in volcano acoustics have enhanced volcanic monitoring, facilitating interpretation of eruption dynamics (e.g., Caplan-Auerbach and McNutt, 2003), explosive volumes (e.g., Dalton et al., 2010; Johnson et al., 2008) and exit velocities (e.g., Vergniolle and Caplan-Auerbach, 2006; Ripepe et al., 2013). An especially important parameter in determining the behaviour of eruption columns is the erupting mass flux (N, Parfitt and Wilson, 2008), which is proportional to the mean exit velocity (U_j):

$$N = \pi r_v^2 \rho_b U_j \quad (1)$$

where r_v is vent radius in m and ρ_b is the gas-magma bulk density in kg m^{-3}. Therefore, a method for determining U_j from volcanic acoustic signals would be of great use in hazard warning and mitigation. Although several acoustic generation mechanisms may exist in volcanic environments, one explored by Matoza et al. (2009) and Fee et al. (2010) is that above-vent sound produced during sustained plume generating volcanic eruptions has similarities to the acoustic signals from industrial jets. Based on empirical aeroacoustic

* Corresponding author.
E-mail address: e.swanson@nhs.net (E. Swanson).

https://doi.org/10.1016/j.jvolgeores.2018.08.005

Nomenclature

A	spreading rate
B	centre line velocity decay
SPL	sound pressure level
St_p	peak Strouhal number
TI	local turbulence intensity
TI_c	centreline turbulence intensity
U	local mean velocity
u'	RMS fluctuating velocity component
U_c	mean centre line velocity
U_j	mean jet exit velocity
U_{jc}	mean jet exit velocity (PIV)
U_{jp}	jet exit velocity (Pitot)
x	axial co-ordinate
x_c	axial extent of the potential core
x_o	jet virtual origin
y	radial co-ordinate
Δf_{12}	frequency band
ρ_b	gas-magma bulk density
ν	kinematic viscosity of air
RMS	root-mean-squared
r_v	vent radius
D	nozzle exit diameter
f_0	fundamental frequency
f_1, f_2	frequency band limits
f_p	peak frequency (measured)
f_{pe}	expected peak frequency
f_{St}	Doppler shifted peak Strouhal number
K	empirical fit parameter
L	length
L_c	corrected length
N	mass flux
NIF	near-to-intermediate field
PIV	particle image velocimetry
P_{ref}	reference pressure, 10^{-6} Pa
P_{rms}	root-mean-square pressure
PSD	power spectral density
Re	Reynolds number
c	sound speed

relationships, this link to industrial jets offers a scaling law between the peak frequency of the volcanic infrasound signal pressure and U_j. Derived from studies of relatively well structured, self-similar jet flows, the empirical jet noise spectra of Tam et al. (1996) show that (a) sound pressure level (SPL) depends on U_j, (b) the signal amplitude and frequency content are directional, and (c) the peak Strouhal number (St_p) depends on emission angle.

The established body of work on the acoustics of industrial jets provides a potential framework for interpreting volcanic infrasound signals but there are key assumptions as discussed by Matoza et al. (2013), that might not be valid, including the dominance of an above-vent sound source, and the similarity in jet flow structure for the jet-engine and volcanic eruption column cases. These assumptions may not be valid because volcanoes have nozzle (i.e. volcanic vent) geometries that differ substantially from jet engines, and unlike jet engines volcanoes have not been engineered to remove sound sources upstream of the vent.

Before proceeding further it is important to clarify terminology. The term 'jet noise' has been applied to acoustic signals associated with a range of volcanic eruptive behaviours, which do not necessarily derive from flows of the same structure as the engineering jets studied, and therefore the associated acoustics relations also may not hold. Taddeucci et al. (2014) state: "For volcanological applications, jet noise can be defined as the characteristic acoustic field generated by a high-velocity jet of gas (with or without a solid and liquid component) entering the surrounding atmosphere and includes multiple source processes and characteristic signals". However, in the aeroacoustics literature (and in this paper), 'jet noise' is the sound generated by turbulent structures within a steady state jet flow, and what Taddeucci et al. (2014) call 'volcanic jet noise' would be considered 'aeroacoustic noise' (of which 'jet noise' is a subset) by the engineering community. Matoza et al. (2009) and Fee et al. (2010) have focused on applications to relatively steady column-generating eruptions but even these may differ in character from the well-structured jet flows on which the relationships are derived, a key consideration being the possible lack of jet potential core in the volcanic case. This region, key for flow establishment, is only seen in jets issuing from contraction nozzles (Ball et al., 2012).

A substantial body of work by the jet research community has demonstrated the effect of initial conditions on jet self similarity (e.g., Fellouah et al., 2009), which will in turn impact noise generation mechanisms. Variations in nozzle geometry have significant effects on the emitted flows, particularly in the region before (i.e. upstream of where) self-similarity has been achieved. This near-to-intermediate field (NIF) is the predominant region of jet noise production (e.g., Papamoschou, 2011). Therefore, alterations to the flow profile in this region have implications for the generation of acoustic signals. The consequences for interpreting volcanic acoustics may be substantial due to the stark contrast between the geometries of engineered nozzles from which the empirical jet noise spectra were obtained and the structure of volcanic conduits and vents.

Noise testing in the engineering setting employs substantial measures to eliminate all but the jet noise source from the recorded data. In particular, nozzles are designed to promote laminar flow on exit and reduce flow separation at the nozzle lip. In addition, the upstream test section is heavily engineered to reduce the transmission of internal noise sources through the test rig (e.g., Bridges and Brown, 2006). Such acoustic treatment is not present in the volcanic setting meaning signals generated will be a composite of all internal and external sound generation mechanisms.

This paper presents results from a series of laboratory experiments designed to assess the sensitivity of jet noise signatures to nozzle geometry. This was achieved by measuring acoustic signals from flows through a set of nozzles with basic geometries, while using particle image velocimetry (PIV) to provide details of the flow structure. An important difference from classical subsonic engineering experiments is the inclusion of divergent nozzles which are more relevant to divergent volcanic vents (Wilson et al., 1980) than straight or convergent nozzles. The investigations included an assessment of our ability to resolve jet operating parameters, via the empirical power spectra, derived from engineering studies (e.g., Tam et al., 1996) when acoustic signals contain both turbulent jet noise and other signals pertaining to the jet rig.

2. Methods

2.1. Experimental apparatus

The experimental apparatus consisted of a settling chamber, baffle cylinder, nozzle test section and acoustically-treated housing. A schematic diagram of the overall design is shown in Fig. 1a.

Compressed air was provided via a regulator from a standard 7 bar fixed airline. Desired volume flow rates were achieved using a convergent-divergent nozzle attachment (designed following Wang and Devenport, 2001), fitted to the rig side of the air regulator. Upon entering the apparatus air flowed through a cubic 0.4 m^3 settling

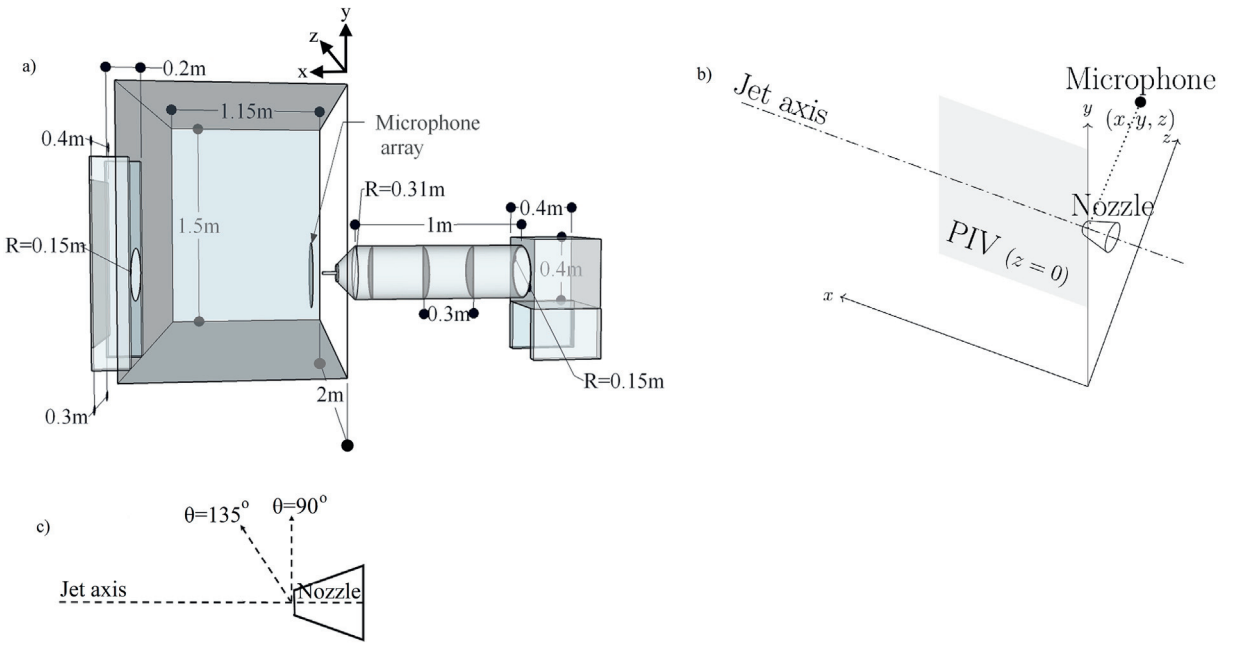

Fig. 1. Experimental setup. A. View from perspex ($z = -0.5$ m) end of the test chamber. Air flow entered the settling chamber (right most section) and passed through baffle cylinder containing 3 baffles before passing through a honeycomb section and entering the test chamber. The disk inside the chamber shows the approximate position of the microphone array. The circular exit vent in the rear wall is indicated by its radius label $R = 0.15$ m. b) Schematic of the PIV test setup. This setup permitted imaging of the along axis jet cross section. The region of the test chamber illuminated by the laser sheet (in the x-y plane) is indicated by the grey plane. During the acoustic tests the Plexiglas windows were covered with Velcro mounted acoustic foam to prevent reflections from these surfaces. c) Orientation of angular measurements from the jet axis. The dashed horizontal line shows the jet axis. Acoustic recordings were made with all microphones in the region where the emission angle (θ) $< 100^{\circ}$.

chamber into a 1 m long × 0.3 m diameter polyvinyl chloride (PVC) baffle cylinder. Three PVC 0.3 m diameter, semi-circular baffles were fitted at 0.3 m intervals within the cylinder and arranged to prevent direct noise transmission between the settling chamber and test section. The settling chamber, baffle cylinder and baffles were lined with 12 mm Fireseal Class 0 Acoustic Foam. A 3.2 mm wide by 20 mm long honeycomb section at the end of the baffle cylinder straightened the flow prior to it entering the convergence which led to the test section. The converging section provided a smooth taper from the 0.3 m diameter cylinder to the 0.1 m diameter test section entrance over 0.1 m. The tests were performed in a 2 m wide × 1.15 m long × 1.5 m high plywood, Comfortex Acoustics, Acoustic Foam Pyramid (AFP)100 mm Acoustic Foam lined chamber (according to the manufacturer apparent absorption coefficient >1 for frequencies >1 kHz). Theoretical calculations give a Schroeder frequency of 550 Hz for the chamber and axial mode resonant frequencies of 170 Hz (width), 273 Hz (length) and 209 Hz (height).

To permit particle image velocimetry (PIV) measurements, a Plexiglas sheet formed the chamber wall at $z = -0.5$ m. This wall was covered with AFP100 mm foam during acoustic tests. The nozzle centre line was located a minimum of 0.5 m from the chamber walls to avoid recirculation effects and a 0.3 m diameter vent in the back wall allowed air to exit the chamber. On the chamber exterior, the vent was shielded by a 0.4 m wide × 0.7 m high × 0.3 m deep AFP100 mm lined cover positioned 0.15 m above the chamber base, fully covering the exit vent. This shield permitted flow to exit, while minimising noise transmission back into the chamber.

2.2. Nozzles

Jet nozzles were attached to the end of the converging section of the baffle cylinder at the junction with the test chamber. Runs were performed at PIV mean exit velocities of 61–140 m s^{-1} using three convergent, five straight and two divergent PVC nozzles (Fig. 2).

The convergent and three of the straight nozzles were 0.08 m long, with 0.005 m, 0.01 m and 0.015 m exit diameters (D). The two additional straight nozzles were 0.12 m long with $D = 0.01$ m; one of these nozzles had a taper at the upstream end which slightly altered the flow entry into the nozzle. The inlet:outlet diameter ratios of the divergent nozzles were 1 : 2 and 1 : 32; both were 0.08 m long with divergence angles of 3.6°. Differing nozzle geometries were used to alter the exit flow structure and so assess the effect on sound generation and transmission. The full range of velocities were not performed for all nozzle geometries because of limitations in the deliverable flow rate. These flow constraints were also the reason for the limited taper of the divergent nozzles.

Following the aeroacoustic jet noise scaling, the expected peak frequency (f_{pe}) for a jet exiting at U_j is

$$f_{pe} = {}^{f_{St}U_j}/_{D}, \quad (2)$$

in which f_{St}, is the observed peak Doppler-shifted Strouhal number. f_{St} depends on observation angle (θ; Fig. 1e) and for narrowband data $f_{St} = 0.3$ at $\theta = 90^{\circ}$ (e.g., Gaeta and Ahuja, 2003; Viswanathan, 2004). The f_{pe} values for each D, U_j combination tested in this study are given in Table 1.

2.3. Experimental runs

For each condition, prior to the first run, an Aerotech pitot tube was placed in the same position with its opening 0.1 m in front of the nozzle exit (between $x = 0.7D$ and $2D$ depending on the nozzle diameter). The regulator was then adjusted so that the pitot tube exit velocity (U_{jp}) was set to 60, 80, 100, 120 or 140 m s^{-1} (measured flow rates fluctuated +/− 5 m s^{-1} around U_{jp}),

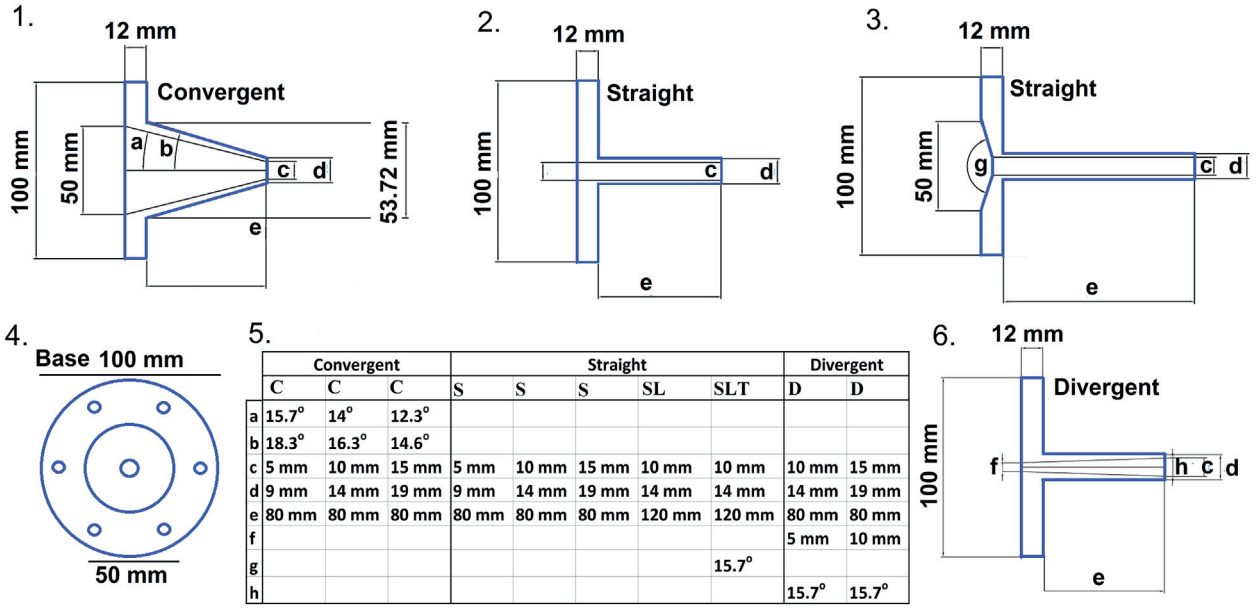

	Convergent			Straight					Divergent	
	C	C	C	S	S	S	SL	SLT	D	D
a	15.7°	14°	12.3°							
b	18.3°	16.3°	14.6°							
c	5 mm	10 mm	15 mm	5 mm	10 mm	15 mm	10 mm	10 mm	10 mm	15 mm
d	9 mm	14 mm	19 mm	9 mm	14 mm	19 mm	14 mm	14 mm	14 mm	19 mm
e	80 mm	80 mm	80 mm	80 mm	80 mm	80 mm	120 mm	120 mm	80 mm	80 mm
f									5 mm	10 mm
g								15.7°		
h									15.7°	15.7°

Fig. 2. Designs for the nozzles used in the experiments. 1) Convergent nozzles (C). 2) Straight nozzles (**S** — straight, **SL** — straight, extended length). 3) Straight nozzle, extended length and internal taper (**SLT**). 4) Nozzle base section. 5) Table of nozzle measurements. Measure c is the nozzle diameter, *D*. Angle g is the angle of taper at the **SLT** nozzle inlet and angle h is the internal angle of the divergent nozzle. 6) Divergent nozzles (**D**). Nozzle identifier letters (**C**, **S**, **SL**, **SLT**, **D**) are used in Table 1 and later figures.

the regulator was then locked and the pitot tube removed before commencing experimental runs with either PIV or microphones. Use of the Pitot tube ensured consistency of flow delivery for experiments comparing different nozzles and also between PIV and acoustic tests. In-chamber temperature was recorded for each run group with an accuracy of $+/-0.5\ ^{\circ}$ C.

2.3.1. Particle image velocimetry (PIV) system

Two-component two-dimensional PIV measurements were conducted using a Dantec Dual Power pulsed 200 mJ laser at 10 Hz repetition rate. Seeding consisted of an atomised mixture of water and Polyethylene glycol-80 providing typical tracer diameters of 1 μm. Prior to running PIV experiments, the acoustic chamber was filled

Table 1
Run conditions and parameter values. Convergent nozzles (**C**), straight nozzles (**S**) and divergent nozzles (**D**). **SL** is the 0.12 m straight nozzle and **SLT** is the 0.12 m straight nozzle with an inlet taper. The expected peak frequency f_{pe} is derived from Eq. (2). f_p is the measured peak frequency. B and x_o describe the centre line decay and jet virtual origin and are obtained from Eq. (3). A and K describe the spreading rate and are determined from Eq. (6). TI_{max} is the maximum turbulence intensity (TI, calculated from Eq. (5)) and $TI_{max}, x\,D$ is its location. HPBW values in italics are those for which there was more than one HPBW peak within the source region.

Shape	D	U_{jp}	U_{jc}	f_{pe}	f_p	x_c/D	x_0/D	B	A		K		TI_{max}	TI_{max}	HPBW
	m	m s^{-1}	m s^{-1}	Hz	Hz				$10 < x/D < 20$	$x/D > 15$	$10 < x/D < 20$	$x/D > 15$		$x\,D$	m
C	0.005	60	71	4260	9563	7.0	−1.78	6.80	0.076	0.084	−4.56	−21.76	0.10	11.4	0.035
C	0.005	80	91	5460	9938	7.0	−1.61	6.82	0.075	0.084	−3.69	−22.55	0.10	10.6	*0.025*
C	0.005	100	97	5820	9375	7.0	−2.34	6.53	0.075	0.084	−4.01	−27.00	0.11	11.0	0.005
C	0.005	120		7200	9281										0.005
C	0.005	140		8400	10,125										0.005
C	0.010	60	63	1890	8531	6.8	−0.08	7.57	0.073	0.073	1.94	1.42	0.12	10.0	0.018
C	0.010	80	84	2520	1734	6.9	0.30	7.78	0.072	0.078	4.87	−19.61	0.13	11.0	0.013
C	0.010	100	98	2940	2344	6.9	0.24	7.60	0.073	0.085	−4.00	−44.85	0.13	10.4	0.008
C	0.015	60	61	1220	1734	6.6	−1.03	6.51	0.078	NaN	−28.41	NaN	0.14	10.4	0.025
D	0.010	60	63	1890	2016	0.9	1.96	5.10	0.081	0.086	13.05	−6.14	0.13	4.6	0.025
D	0.010	80	95	2850	3844	1.0	1.53	4.78	0.084	0.090	7.90	−14.34	0.12	5.4	*0.01*
D	0.010	100	113	3390	3703	1.0	1.33	4.60	0.087	0.085	5.93	12.57	0.12	5.4	0.005
D	0.010	120		3600	7031										0.005
D	0.015	60	67	1220	1969	1.1	2.52	5.78	0.096	NaN	34.47	NaN	0.15	4.9	0.005
S	0.005	60	69	4140	7969	5.4	−1.70	5.97	0.073	0.085	−8.10	−35.01	0.09	9.6	0.025
S	0.005	80	89	5340	7922	5.8	−1.92	5.96	0.075	0.085	−11.01	−33.71	0.09	10.5	0.014
S	0.005	100	89	5340	11,719	5.8	−2.35	5.75	0.072	0.086	−5.65	−36.65	0.10	10.4	0.0045
S	0.005	120		7200	11,578										0.005
S	0.005	140		8400	11,156										0.006
S	0.010	60	68	2040	3891	5.4	0.10	6.90	0.071	0.063	2.02	34.89	0.12	9.0	0.02
S	0.010	80	86	2580	7547	5.2	−0.08	6.71	0.074	0.080	−1.25	−19.81	0.12	8.5	0.015
S	0.010	100	98	2940	7406	5.1	0.70	7.11	0.074	0.072	3.67	12.57	0.13	9.7	0.006
SL	0.010	80	89	2400	7734										0.015
SLT	0.010	80	89	2400	6750										*0.015*
S	0.015	60	63	1260	3750	2.4	2.09	7.36	0.060	NaN	93.49	NaN	0.13	8.2	0.0045

with seeding to minimise correlation bias errors near the jet edge. The laser housing was positioned on a Plexiglas sheet located in the test chamber roof, with the laser sheet aligned to illuminate the vertical plane containing the jet axis (Figs. 1b and 3).

The camera was positioned facing the Plexiglas wall of the test chamber in order to image the cross section of the jet in the illuminated plane. Scattered light intensities were recorded using a HiSense 11M camera yielding 4000×2672 pixel images, with a typical resolution of 24.4 pixels/mm. Processing was performed using correlation windows of 16-by-16 pixels with a window overlap of 50% translated in a vector spacing of 0.37 mm and spatial resolution of 0.74 mm ($=1/16$ pixels). The total area processed is 186×124 mm in the x,y plane (Fig. 1b). For each nozzle a total of 1600 image pairs constituted the database for statistical analysis with each image spanning approximately $30D$ downstream for the $D = 0.005$ m nozzles. One image pair was collected every 0.1 s, providing statistically independent flow fields. For each image pair the pixel shift of the seeding tracers between the first and second laser pulses was used to calculate the jet flow parameters. Individual recordings within each image pair were separated temporally by 60 μ s, equating to a maximum particle image displacement of 8 pixels. This setting ensured a reliable outcome of the image processing and is generally accepted to yield an optimum trade-off in dynamic PIV measurement range and robustness. Given an estimated maximum fluctuation in local velocity (i.e. local root-mean-squared (RMS) velocity/velocity) of 25%, discrepancies in mean velocity and turbulence intensity are estimated at ±1.2% and ±0.8% nozzle velocity respectively for a 95% confidence level, assuming normal distributions in error. The accuracy of the PIV measurement system decreases as velocity increases due to the increased pixel shift per frame. PIV measurements were therefore only done for experiments with U_{jp} up to 100 m s^{-1}. A series of calibration images were taken to establish the dimensions of the PIV images and estimate the pixel-to-mm conversion factor. Additionally a series of seed-free, flow-free background images were recorded, averaged and then subtracted from each PIV run to remove any residual background motion or path effects, thereby improving the reliability and accuracy of the obtained results.

2.3.2. Acoustic tests

Acoustic signals were recorded at 96 kHz with a GFaI acoustic camera acquisition system, using an array of 36 microphones evenly distributed along the perimeter of a circle of 0.35 m diameter. According to the manufacturer, the microphones have a flat frequency response to 20 kHz. While beamforming at higher frequencies is possible as all of the microphones have the same frequency roll-off, absolute pressure values at frequencies >20 kHz are not valid. For pure jet noise the recorded frequency spectrum varies with observation angle (e.g., Gee et al., 2013), so measurements were made with the plane of the array aligned near-perpendicular to the jet axis. This alignment positioned the maximum number of microphones $\theta < 100^{\circ}$ from the jet axis (Fig. 1c) and enabled beamforming of signals relating to the low angled acoustic spectra discussed by Tam et al. (1996). To allow different regions of the jet to be resolved using beamforming, the microphone array was positioned at distances $< 200\ D$ from the jet axis. The positions of a subset of three microphones were measured and used to determine the full array locations prior to analysis. Array calibration was performed using two 0.01 m diameter headphones mounted on a rod along the nozzle axis.

For each flow condition acoustic recordings were made of five 8-second runs for all applicable nozzles; the duration was set in order to ensure the flow reached a steady state. Acoustic recordings started one second prior to opening the flow valve giving 8-second runs consisting of 1 s of background (noise) and 7 s of flow (signal). The low flow rate limit was set as the minimum to generate a signal distinguishable, by eye, in the acoustic traces, while the upper limit was defined by the maximum deliverable air flux.

Steady flow conditions were achieved after 4 s, based upon the variance reduction in spectrograms of the acoustic recordings. Therefore, spectral analyses were performed upon seconds 6 to 8 of the samples for all microphones in the required angular region. Acoustic sources were located using a delay-and-sum beamformer (Olson and Szuberla, 2008) and the Power Spectral Density (*PSD*) estimates for the peak source locations were made using a 2048 point Digital Fourier Transform with 50% overlap, giving a frequency resolution of 46.9 Hz.

3. Results — particle image velocimetry

A series of jet parameters was extracted from the PIV data to ensure the jets tested were comparable to those reported by previous studies (e.g., Fellouah et al., 2009; Quinn, 2006) and also to relate the acoustic results to the jet flows. The parameters were the mean exit, centre line and local velocities (U_{jc}, U_c, U), local RMS fluctuating velocity (u'), axial extent of the potential core (x_c), local and centre line turbulence intensity (TI, TI_c), centre line velocity decay parameter (B) and spreading rate (A). Results are summarised in Table 1. While previous studies have concentrated on the intermediate-field and fully-developed region, this study focused on the near-to-intermediate-field (NIF) as this is the region predominately responsible for sound generation (e.g., Papamoschou, 2011).

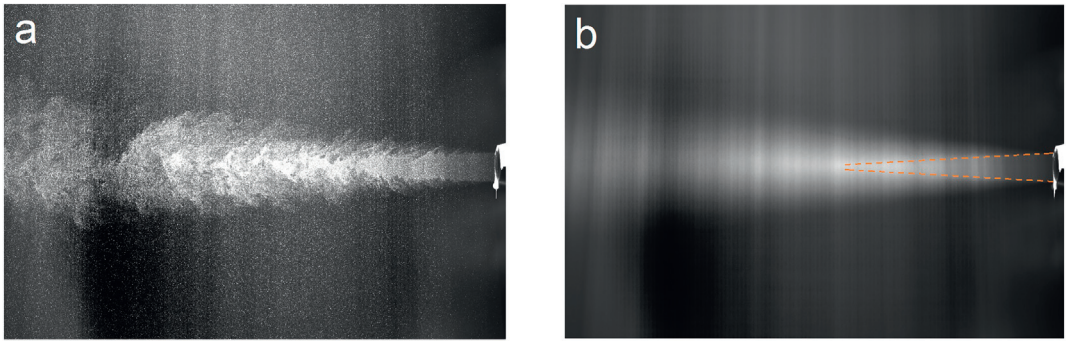

Fig. 3. 2 HiSense 11M camera images from a 0.01 m diameter, convergent nozzle test performed with $U_j = 60$ m s^{-1}. a) A single instantaneous image. b) The time average of 10 image pairs in which the jet potential core is highlighted by red dashed lines.

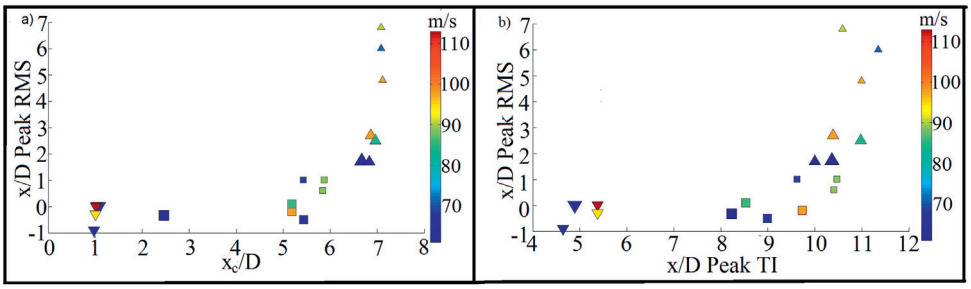

Fig. 4. a)x/D peak beamed *RMS* pressure location versus x_c/D for runs with both PIV and acoustic results. b) x/D peak beamed *RMS* pressure location versus x/D peak *TI* location for runs with both PIV and acoustic results. Convergent nozzles:△, straight nozzles: □ and divergent nozzles: ▽. Small, medium and large symbols represent the 0.005 m, 0.01 m and 0.015 m diameter nozzles respectively. The nozzle exit is located at $x = 0$. Plotted velocities are taken from the PIV measurements (U_{jc}). Peak *RMS* pressure locations for the convergent 0.005 m diameter $U_{jp} = 120\,\mathrm{m\,s^{-1}}$, $140\,\mathrm{m\,s^{-1}}$ and straight 0.005 m diameter $U_{jp} = 120\,\mathrm{m\,s^{-1}}$, $140\,\mathrm{m\,s^{-1}}$ nozzles were x/D =5, 5.6, 0.2 and 0.6 respectively. These data are not plotted as PIV data are not available at these velocities.

3.1. Potential core

The axial extent of the potential core (x_c, x being the axial coordinate with $x = 0$ located at the nozzle exit) was taken to be the point at which $U_c = 0.95U_{jc}$ (e.g., Grandchamp and Hirtum, 2013). The x_c, normalised by D (x_c/D), was approximately constant for all nozzles within a geometry type (straight, convergent, divergent) except the straight $D = 0.015$ m nozzle (Fig. 4a).

The extent of the potential core was longest for convergent nozzles (mean $x_c/D = 6.9$, $\sigma = 0.1$) and shortest (further upstream) for the divergent geometry (mean $x_c/D = 1.0$, $\sigma = 0.1$). The results from the straight $D = 0.015$ m nozzle stood out from other straight nozzle tests due to: an upstream shift in x_c/D, increase in peak Turbulence Intensity (*TI*, Section 3.3) and the lowest spreading rate of all tests. Values for the individual runs are given in Table 1. The x_c locations for the convergent and divergent nozzles were in agreement with those of Arakeri et al. (2003). Excluding the $D = 0.015$ m nozzle measurement, the mean x_c for the straight nozzles was $x_c/D = 5.5$ ($\sigma = 0.3$).

3.2. Velocity profiles

The divergent nozzles had consistently Gaussian radial velocity profiles at $x/D = 2$ (Fig. 5a) but jets from the straight and

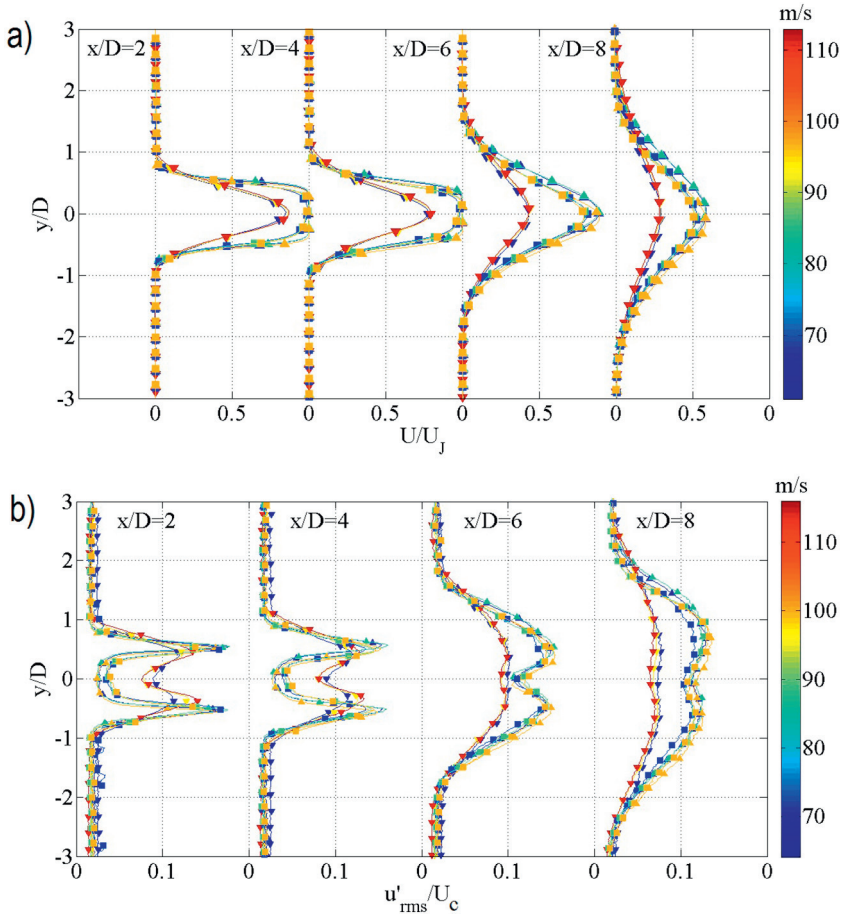

Fig. 5. a) Downstream evolution of the radial velocity profiles for the 0.01 m nozzles. b) Downstream evolution of the radial turbulence intensity profiles for the 0.01 m nozzles. Convergent nozzles: △, straight nozzles: □ and divergent nozzles: ▽.

convergent nozzles had less developed profiles on exit. Grandchamp and Hirtum (2013) used three theoretical pipe flow profiles to describe jet exit velocity regimes: the parabolic (fully developed laminar pipe flow), $\frac{1}{7}$ power law (turbulent pipe flow), and the hyperbolic tangent ('top hat') profiles. While for our experiments with straight nozzles the flow regime at $x/D = 2$ was best matched by the 1/7 power law (turbulent) pipe flow profile, the convergent nozzles $x/D = 2$ regime matched the top hat profile. For both the straight and convergent nozzles, radial velocity profiles did not become Gaussian until several nozzle diameters downstream of the exit.

U_{jc}/U_c increases systematically with downstream distance. This decay can be related to jet virtual origin position (x_o) and an empirical parameter B associated with the nozzle shape,

$$\frac{U_{jc}}{U_c} = \frac{1}{B}\left(\frac{x - x_o}{D}\right) \tag{3}$$

(e.g., Fellouah et al., 2009). B and x_o were obtained through a least squares regression fit of data in the region $x > 1.5x_c$. B values for the convergent and straight nozzles (Table 1) were slightly higher than those reported previously (Table 2), which are typically for the fully developed flow region ($x/D > 30$), whereas in our experiments maximum x/D values were 32, 18 and 11 for the $D = 0.005$ m, $D = 0.01$ m & $D = 0.015$ m nozzles respectively. Fellouah et al. (2009) reported that in the intermediate field ($x/D < 30$), the centre line decays faster than in the self-similar (fully developed) region, which can explain our relatively low B values. Interestingly, the B values for the divergent nozzle were more consistent with previous results (for fully-developed flows), falling in the range 4.6–5.8. The reduction in B values from convergent through straight to divergent geometry is an indication of increasingly developed flow at the jet exit. These results, along with the shorter extent of the potential core, suggest that a jet starts to develop inside the divergent nozzle, which is also consistent with the downstream shift in x_o from divergent relative to the straight and convergent nozzles (Table 1). Values of x_o for the straight and convergent nozzles obtained from a best fit of Eq. (2) increased with Reynolds number (Re),

$$Re = \frac{D \times U_{jc}}{\nu}. \tag{4}$$

Here, the kinematic viscosity of air (ν) is defined using standard atmospheric pressure (101,325 Pa) at 20 °C. In contrast the divergent results appeared Re independent with $x_o/D \approx 2$, though the data are limited.

3.3. Turbulence intensity (TI)

Following Quinn (2006), TI and TI_c are defined as,

$$TI = u'/U_c,\ TI_c = u'/U_{jc}. \tag{5}$$

The TI_c values here correspond to those reported by Raman et al. (1994). For $x/D \leq 16$ the behaviour of the divergent nozzle curves differed from the other nozzles, with TI_c significantly larger. For the $D = 0.005$ m and $D = 0.01$ m convergent and straight nozzles the TI_c increased rapidly to $x/D \approx 10$, the TI_c peak occurring first for the straight nozzles. Following this, the TI_c curves decreased gradually with the two geometries becoming similar at $20 < x/D < 30$. Due to the limited data it was not possible to assess the $D = 0.015$ m nozzles in the $x/D \approx 20 - 30$ region.

For each experiment, the peak TI_c value and location was determined from a $TI_c(x)$ curve smoothed with a 100-sample moving average. As with the x_c locations, the peak TI_c locations from closest to the nozzle exit to furthest downstream corresponded to the divergent, then straight then convergent nozzles. Using direct numerical modeling, Bogey et al. (2008) showed that the peak in centre line turbulence intensity is located between 1D and 2D downstream of the potential core, the distance increasing with increasing initial turbulence. The TI_c peaks from this study were 3.3–4.7 D downstream of x_c. However, the peak region extended over at least 1 jet diameter.

Considering the full axial TI_c profiles, the divergent nozzles had the largest TI_c values to $x/D \approx 5$ and these remained larger than the convergent nozzles to $x/D \approx 6$. For $x/D \geq 10$, TI_c was greater for the convergent than the straight nozzle.

The downstream evolution of radial TI for the $D = 0.01$ m nozzles is shown in Fig. 5b. In these profiles, considered representative of all diameters, there is a clear difference in the behaviour of the divergent compared to the straight and convergent nozzles. Within each nozzle geometry category (straight, convergent, divergent) the radial TI profiles became similar for $x/D > 13$. The mean radial location for peak TI at $x/D = 2$ for the convergent nozzles was $y/D = 0.56(\sigma = 0.02)$, y being the radial coordinate. In agreement with the convergent nozzle experiments of Lau et al. (1979) this was also the location at which $U = U_{jc}/2$. For the straight nozzles the peak location reduces to $y/D = 0.51(\sigma = 0.03)$ and for the divergent nozzles the peak shifted closer again to the jet axis $y/D = 0.41(\sigma = 0.09)$.

3.4. Spreading rates

The spreading rate, A, is defined as $\partial b\, \partial x$ where b is the radial position at which $U = U_{jc}/2$ (e.g., Rajaratnam, 1976). A values (Table 1) were obtained via a least squares linear regression of

$$\frac{b}{D} = A\frac{x}{D} - K \tag{6}$$

(e.g., Ball et al., 2012), with K an empirical fitting parameter. Where possible, A was calculated for $x/D > 15$ which is the region at which spreading rate is linear (Ball et al., 2012). The mean values were: convergent nozzles, 0.081 ($\sigma = 0.005$), straight nozzles, 0.078 ($\sigma = 0.003$), divergent nozzles, 0.087 ($\sigma = 0.009$). Although not ideal, A values were also determined for the $10 < x/D < 20$ region for all experiments due to the lack of data at $x/D > 15$ for $D = 0.015$ m nozzles. Our values compare well with previously reported spreading rates (Table 2).

4. Results — acoustic measurements

In all cases, the delay-and-sum beamformer returned a single elongate source region. The Half Power Beam Width (HPBW) was calculated using the lateral extent of regions for which the RMS Pa value was < 3 dB below peak RMA Pa. The mean HPBW values for each run are presented in Table 1. The convergent $D = 0.005$ m, $U_j = 80$ m/s, straight $D = 0.01$ m, $U_j = 80$ m/s and straight, taper $D = 0.01$ m, $U_j = 80$ ms^{-}1 source lobes contained two HPBW peaks. For these runs, the HPBW given is the total expanse of these peak regions. The peak RMS pressure locations for the divergent nozzles were located in the region of the nozzle exit ($x/D = 0$, Fig. 4a). The potential cores of these flows were short ($x_c/D \approx 1$), with peak TI locations in the region of $x/D = 5$ (Fig. 4b). For the $D = 0.01$ m and $D = 0.015$ m straight nozzles the peak RMS pressures were located in the region of the nozzle exit. However, for the $D = 0.005$ m straight nozzles there was a slight downstream shift in the peak RMS pressure location. The acoustic source locations returned for the straight nozzles did not relate to the x_c/D ($5 < x/D < 6$) or peak TI ($8 < x/D < 11$) locations. For the $D = 0.005$ m straight nozzles, it is possible that the downstream shift in location was due to the merging of two sound sources containing a

Table 2
Centre line velocity decay and spreading rate values for previous experiments reported in Ball et al. (2012) and Quinn (2006).

Authors	Nozzle	x/D	x_o/D	B	A
Wygnanski and Fiedler (1969)	Contraction	≤ 50	3	5.7	0.086
		≥ 50	7	5	
Panchapakesan and Lumley (1993)	Contraction	30–160	0	6.06	0.096
Hussein et al. (1994)	Contraction	30–120	2.7	5.9	
Weisgraber and Liepmann (1998)	Contraction	17–27	0	6.7	
Ferdman et al. (2000)	Pipe	≤ 15	2.5	6.7	
Mi et al. (2001)	Contraction	0–64	3.5	4.48	
Xu and Antonia (2002)	Contraction	20–75	3.7	5.6	0.086
Quinn (2006)	Sharp-edged orifice	18–55	2.15	5.99	0.098
	Contraction	18–55	3.65	6.1	0.096
Fellouah et al. (2009)	Contraction	15–29	2.5	5.59	

similar range of frequencies, one emitted from the nozzle and one generated by the jet flow, with the final resolved location being dominated by the stronger sound source. For the convergent nozzles, a greater downstream peak RMS pressure location was returned for the $D = 0.005$ m nozzles compared to the wider diameter nozzles. For the $D = 0.005$ m convergent nozzles there was good agreement between the peak RMS pressure locations and x_c/D, with the peak TI locations around $4x/D$ further downstream. For the $D = 0.01$ m and $D = 0.015$ m convergent nozzles the peak RMS location shifted upstream from x_c/D. As proposed for the straight nozzles this shift may have resulted from the merging of two sound sources. Additional beamforming results, employing a deconvolution technique in an attempt to identify multiple acoustic sources, are consistent with these findings (Appendix B).

Five of the test runs (three straight and two divergent) returned negative peak RMS pressure locations i.e. upstream of the nozzle exit. For the $D = 0.01$ m, $U_{jc} = 63$ m s^{-1} run the shift was the same diameter as the nozzle (2 pixels), while for the other four runs the negative shift is only 1 pixel from the nozzle exit. Sound emitted from ducts can have a complex radiation pattern and part of this shift may be due to fitting a 3D problem to a 2D solution. There may also be minor errors with array calibration. However, even if a two pixel positive shift were applied to all of the results the differences between geometries would remain. For the convergent nozzles, the dominant acoustic source locations related to within-flow processes. In contrast the dominant acoustic sources from the straight and divergent nozzle tests were generated from the nozzle exit region.

The mean Power Spectral Density (*PSD*) curves, created from the beams at the maximum *RMS* location for each run condition, are presented in Fig. 6. The *PSD* is the estimate of the mean squared pressure per unit frequency and the *SPL* value for a given frequency band ($SPL(\Delta f_{12})$) is given by

$$SPL\,(\Delta f_{12}) = 10 \times \log_{10}\left(\frac{P_{rms}^2}{P_{ref}^2}\right), \tag{7}$$

where P_{rms} is the RMS pressure,

$$P_{rms}^2 = \int_{f_1}^{f_2} PSD(f)df, \tag{8}$$

f_1 and f_2 are the frequency band limits and, following convention, the reference pressure (P_{ref}) is taken as 20×10^{-6} Pa (e.g., Garcés, 2013).

Signals from the straight and divergent nozzles were characterised by a series of peaks, which had higher amplitudes than the smoother spectra observed from the convergent nozzles. In all cases, the spectra bore little resemblance to the smooth spectra generated by a pure jet noise signal. The peaks in Fig. 6 above 1000 Hz exceed the Schroeder and resonant frequencies of the test chamber (Section 2.1). Furthermore, as these peaks are not seen for all nozzles they cannot be related to the test chamber, a constant feature of the experiments. As the dominant sound sources were located upstream of x_cD, the spectral characteristics are thought to be controlled by noise generation mechanisms internal to the jet rig. This hypothesis is supported by the relationship between the harmonic resonance tones of the nozzle barrel seen for the straight and divergent nozzles and the nozzle barrel length (Appendix A). Nozzle geometry affected the amplitude of the tones: for divergent nozzles the amplitude of these tones was reduced at higher frequencies compared to the straight nozzles. A similar effect is noted by Rossing (1990) on the impedance curve of a trumpet due to the addition of a bell to the instruments tubing. Signals from the divergent nozzles were consistently stronger than those of the other geometries. Given that the inlet diameter was constant, this demonstrates the amplification effect of a divergent nozzle on any signal transmitted from upstream of, or generated within, the nozzle region; such an effect is well known in regard to the sound transmission in horns (e.g., Kuttruff, 2007).

The peak frequencies (f_p) for the straight and divergent nozzles related to the harmonic resonance tones of the nozzle barrel and did not correlate with the expected peak frequencies (f_{pe}) for the emitted jet flows (Table 1) calculated from Eq. (2). For the convergent nozzles only the $D = 0.01$ m $U_{jc} = 84$ and 98 m s^{-1} and the 0.005 m $U_{jp} = 140$ m s^{-1} runs had f_{pe} similar to the recorded f_p . Considering the set of all the convergent nozzle experiments, f_p is insensitive to U_{jc} and so not useful as a means of returning U_{jc}. As with the straight and divergent nozzle spectra, signals from the convergent nozzles were thought to be heavily influenced by internal noise sources. Importantly, this internal noise influence meant that even where the sound source was located near to the expected dominant jet noise generation region, the frequency characteristics could not be used to infer the jet operating parameters.

5. Discussion

In our experiments, the flow profiles and acoustic source parameters for divergent nozzles were significantly different than for the other nozzle geometries (straight and converging). Experimental (e.g., Solovitz et al., 2014) and real-world (e.g., Wilson et al., 1980) observations show an upward divergence of volcanic vents. This suggests that results from divergent nozzles are more relevant to the volcano-acoustics community than typical aeroacoustic experiments which use convergent or straight nozzle geometries.

The different nozzle geometries generated distinct radial jet velocity profiles. The divergent nozzle exit flow had a Gaussian U_{jc} profile, with the *TI* profiles indicating that the flow was turbulent on exit (Fig. 5). This was in contrast to the straight and convergent nozzles for which the flow properties differed on exit (power law

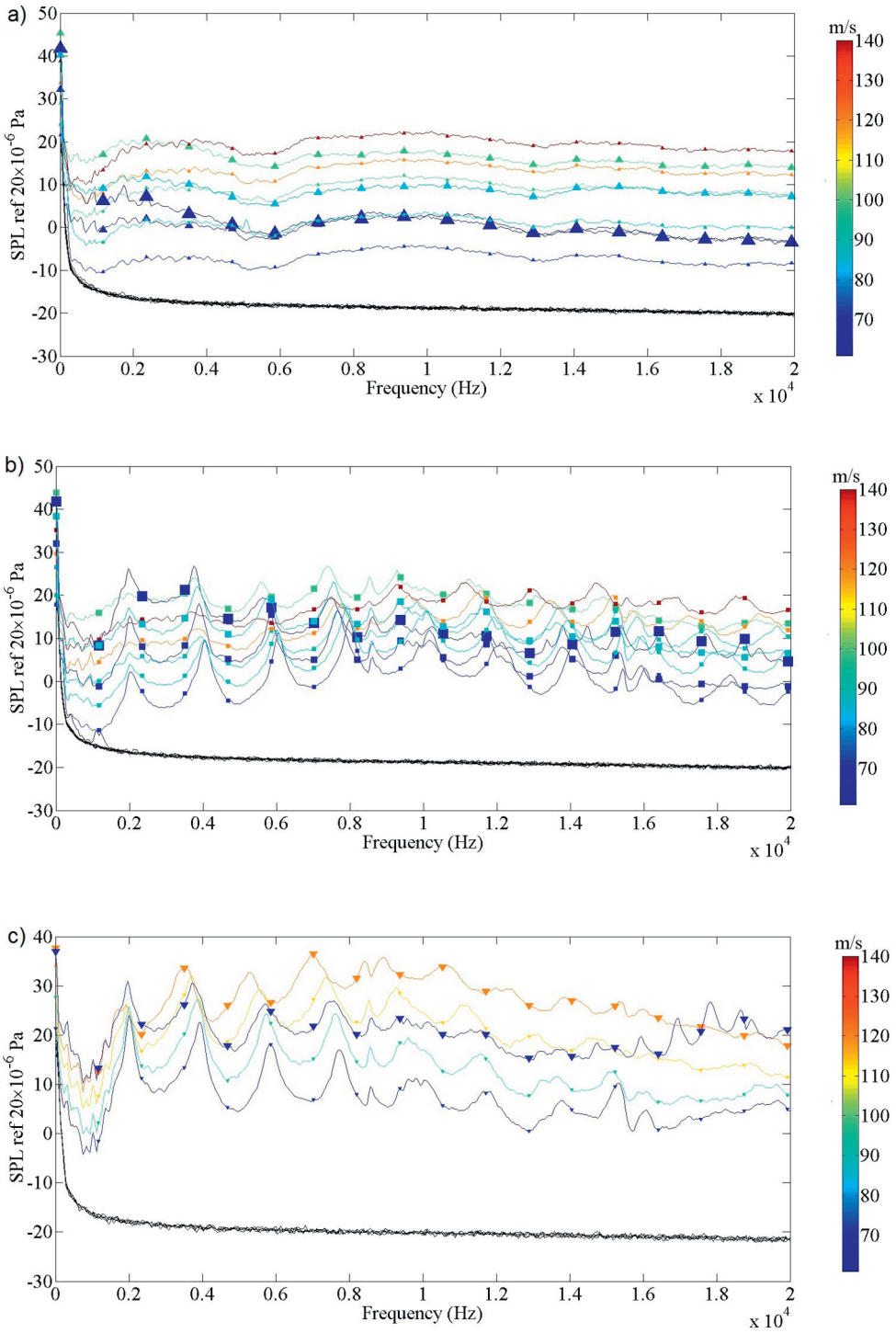

Fig. 6. Mean beam *PSD* curves for the standard runs. a) Convergent runs, *SPL* measured 0.722 m from the nozzle. b) Straight runs, *SPL* measured 0.722 m from the nozzle. c) Divergent runs, *SPL* measured 1.091 m from the nozzle. Black lines indicate the background noise levels.

and top hat radial velocity profiles, respectively) but became similar downstream of the potential core (x_c). The straight and convergent nozzles also produced *TI* profiles that indicated the centre line turbulence intensity increased as the jet developed. It is notable that there were significant differences in results between the divergent and other nozzles even though the divergence angle was only 3.6°. A first order interpretation is that the flow exits the divergent nozzles in a more developed state than typical laboratory or aircraft jets. Being turbulent on exit, surface waves are already present in the shear layers of the divergent jets, whereas standard laboratory jets have a region over which these develop. Such changes in initial conditions will impact acoustic signal generation.

The dominant acoustic source for the divergent nozzles was further upstream than those for the convergent and straight nozzles (Fig. 4). This is consistent with the observed flow regimes: the divergent nozzles exhibited a shorter NIF extent with $x_c/D \approx 1$

(Fig. 4) and produced maximum acoustic power in the region of the nozzle exit. A consequence of this flow structure is that any jet noise signal was masked by a louder internal noise signal generated by air flow through the rig and interacting with the nozzle. Therefore, retrieval of the jet operating parameters from the beamed spectra, using the observed peak frequency and amplitude, was not possible.

The influence of the rig and nozzle noise was not restricted to the divergent nozzles; the straight nozzles also produced harmonic tones. The convergent nozzles did not produce clear harmonic tones and had source regions of significant acoustic power downstream of the jet exit (Fig. 4). These results suggest that the sound generated by the convergent nozzle flow regimes acted to overpower near-nozzle noise generation. Importantly, even with convergent nozzles the acoustic spectral characteristics could not be inverted for jet operating parameters. This suggests that even in these cases the acoustic signature was not dominated by pure jet noise, or that the peak frequency scaling (Eq. (2)) for linking jet to acoustic parameters is incorrect.

The dependence of the flow properties and acoustic signals on nozzle geometry has significant implications for the interpretation of volcano infrasound. Yet, much work remains to understand the differences between the simple experimental setup described in this paper and sustained volcanic eruptions. Matoza et al. (2013) identified a number of issues with scaling laboratory and aircraft measurements to realistic volcanic environments. Here, we briefly describe some of the more pertinent issues with regards our work.

We focused on a simple set of divergent nozzles (Fig. 2 and Table 1) that had a small internal divergence angle of 3.6°; it is unclear what divergence angles would be representative of natural volcanic systems. Models (e.g., Wilson et al., 1980) suggest that the divergence angles may be significantly wider. There is a need for work that focuses on identifying the consequences of widening the divergence angle and adopting a more complex nozzle geometry on the flow and acoustic regimes, and on understanding the acoustic directivity of sound generated by these systems.

The combined effect of the conduit length and the divergence geometry should also be considered. Conduit length alone may have a large influence on the radiated sound. Jet flow experiments of Grandchamp and Hirtum (2013) showed that nozzle length (L) can control the initial flow profile with jets exiting from a long straight pipe ($L/D = 53.2$) exhibiting a developed pipe flow regime with no uniform core region. In contrast, jets exiting from a short nozzle ($L/D = 1.2$) did so in the 'top hat' regime. As fragmentation depths in models of Plinian eruptions (e.g., Polacci et al., 2004) are typically at least an order of magnitude greater that the conduit diameter, a gas flow originating at the fragmentation level of a volcanic vent would be expected to exit in a developed flow regime. Such flows have the same characteristics as we observed for divergent nozzles, and so might be expected to produce significant near-nozzle sound that is largely influenced by internal (rig) noise. The influence of internal noise, and the interplay between conduit processes and the radiated acoustic wavefield, is poorly understood. Recent work by Palacios et al. (2016) suggests that for sustained eruptions at Tungurahua, Ecuador, there is a single, internal source for both the seismic and acoustic wavefields.

There are also issues with scaling of the flow parameters from aeroacoustic experiments to volcanic eruptions. The Reynold's numbers of Plinian eruptions ($10^{10} - 10^{12}$; Valentine and Wohletz, 2012), and those investigated in our experiments are well above those reported in the engineering literature (e.g., Viswanathan, 2004). Although exit velocities of volcanic plumes are comparable to those studied by the aeroacoustic community, the diameters of volcanic vents are of order $10 - 10^2$ m which is much greater than the nozzle diameters of aeroacoustic tests. Viswanathan (2003) showed that for equal mass flow rates the level of internal noise is greater for larger nozzles. In order to match exit velocities for different size nozzles, a greater mass flow is required for the larger nozzle. This increase in mass flow generates greater levels of internal noise. As internal noise increases at a greater rate than turbulent jet noise (Viswanathan, 2004), beyond a rig-specific threshold, internal noise becomes the dominant signal. Therefore, for volcanic exit velocities comparable to the engineering literature the influence of internal noise on the volcanic signal is expected to be significant. This signal could be generated by flow interaction with the conduit walls and vent lip and processes within the vent such as conduit erosion and fragmentation (Fee et al., 2017; McNutt and Nishimura, 2008).

Although our experiments did not generate pure jet noise signals, there was a clear downstream sound source in the convergent nozzle runs. The velocities of our experiments were lower than those commonly studied in subsonic engineering studies and effects at higher velocities warrant further investigation. However, the self-similar nature of our experimental jets for each of the three nozzle geometries means the differences in flow properties noted between the convergent, straight and divergent nozzles would remain at higher velocities. Therefore, the differences between acoustic signal generation mechanisms should also remain. Exit velocities for Plinian eruptions (≈200–600 m s^{-1} Wilson et al., 1980) are comparable to the velocities measured in the engineering setting. However, the velocity, diameter ratio and exit structure all differ between the experimental and volcanic cases with potentially important implications for signal comparison.

The volcanic case is also further complicated by the potential for supersonic flow at the beginning of the eruption. Experiments have shown that choked flow, associated with supersonic conditions, generates a high pitched noise of greater amplitude than the jet noise signal which dominates the acoustic spectra (Powell, 1953). Powell (1953) also highlights the sensitivity of turbulence mechanisms to initial conditions and the need for assessing repeatability before interpreting and applying results. Given the level of uncertainty in volcanic vent geometry and flow properties, care must be taken to not assume a strict correspondence between controlled laboratory acoustic experiments and volcanic infrasound signals.

Models of over-pressurised volcanic eruptions have shown flow expansion post vent exit (Valentine and Wohletz, 1989; Ogden, 2011). Therefore, to apply a model relating vent diameter, exit velocity and a flow-generated acoustic signal the ratio of vent radius to column basal radius must be known. This ratio, determined by the difference between eruptive and atmospheric pressures and the internal angle of the vent (Ogden, 2011), varies both between and over the course of individual eruptions. A further complication of over-pressurised volcanic jets is that the central jet may be surrounded by an annular region of unsteady, non-uniform flow (Ogden et al., 2008). The acoustic signal created by this region has the potential to be stronger than the jet noise associated with turbulent mixing and so dominate the apparent jet noise spectrum.

Although Matoza et al. (2009, 2013) explored the hypothesis that above vent noise generation mechanisms could help explain the characteristics of infrasound recorded during sustained explosive eruptions, they recognised that other volcanic fluid flow processes (e.g., multiphase flow, interaction with the shallow conduit structure and vent walls, volcanic jet eroding a vent and/or crater) may also produce measurable signals. Our results indicate that vent and conduit processes are likely to be significant generators of volcanic infrasound, producing signals in the vent region. This is not to argue that there is no signal generated by the above-vent flow, but rather that this signal may be overwhelmed by signals generated at or within the vent. A combination of laboratory experiments and well designed field deployments (e.g., Rowell et al., 2014) will be required to identify and separate the major acoustic sources. Therefore, before

infrasound data can be confidently inverted for sustained eruption parameters, a thorough assessment of the influence of in-conduit processes on volcano-acoustic signals is required.

6. Summary

Our results demonstrate the influence of nozzle geometry on the flow structure of emitted jets. Jet flows from convergent nozzles possessed structural features related to the generation of aeroacoustic jet noise. In contrast, flows from divergent nozzles, which are of greater relevance to volcanic vents, exited in a developed flow regime with a significantly shorter potential core length. In these divergent nozzle tests, for which $x_C/D \approx 1$, it was not possible to distinguish between internal and flow generated acoustic signals. Even in the case of the convergent nozzle tests, the combination of internal and external sound sources prevented the identification of the jet operating parameters from the acoustic signals. Further experimental work is needed to investigate the acoustics of divergent jets and also to develop robust methods for separating internal and external sound signals.

In the volcanic case, the nozzles (vents) have no acoustic treatment meaning internal sound will contribute to the emitted acoustic signals. In addition, the flow structures of volcanic eruptions are more complex than the simple jet flows examined by our experiments. Therefore, eruption parameters retrieved from volcanic signals using existing jet noise theory cannot currently be relied upon. Decades of high-end engineering research led to the development of jet noise theory for nozzle and flow combinations which are simple in comparison to the volcanic problem. Given the potential consequences of incorrect inversion of volcanic signals, substantial experimental investigation tailored to volcanic issues is required.

Acknowledgments

This research was funded by a UK NERC PhD studentship and NERC GrantNE/G016593/1. We thank Robin Matoza and an anonymous reviewer for their comments which improved this manuscript. Data Access Statement all underlying data are described and provided in full within this paper.

Appendix A. Nozzle tones

Strong tonal peaks were observed in the divergent and straight spectra (Fig. 6). The frequencies of the observed tones can be directly related to the nozzle dimensions, so the tonal features are considered to be generated by the nozzle geometry. The fundamental frequency (f_0) of an open ended straight pipe is given by:

$$f_0 = {}^{c}/_{2L_c}, \tag{A.1}$$

where c is sound speed and L_c is the corrected pipe length (e in Fig. 2),

$$L_c = L + 2(0.305\ D), \tag{A.2}$$

L being the length (e.g., Rossing, 1990). The first five clearly-visible peaks >1 kHz from the straight and divergent nozzles were identified manually and are plotted against Re in Fig. A.1a and b, with the effect of nozzle length shown in Fig. A.1c.

With the exception of $Re = 46{,}481$, for $D = 0.005$ m, the theoretical tonal peaks calculated using Eq. (A.1) were a good match to the observed data, though in some cases the fundamental was missing. The good fit for the divergent nozzles was due to the minimal taper used.

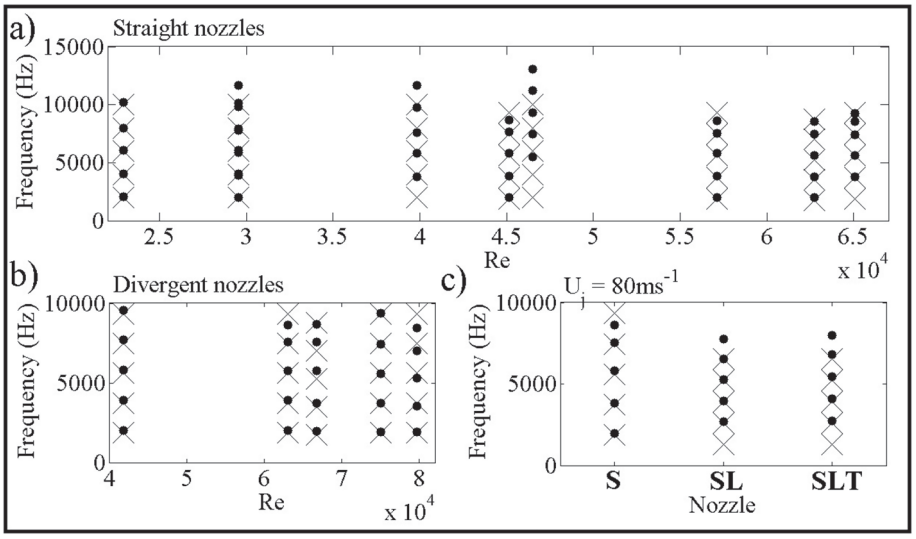

Fig. A.1. Frequencies of tonal peaks for the straight (a), divergent (b) and varied length, straight (c) nozzles. In Figure c, **S**- straight, **SL**-straight, extended length, **SLT**-Straight nozzle, extended length and internal taper. Recorded values are indicated by dots. The predicted first 5 harmonic frequencies are plotted as crosses for each case. The x-axis labels for (c) indicate which of the straight nozzles were used. See Fig. 2 for details of nozzle geometries.

Appendix B. Adaptive beamforming results: CLEAN

To extend the delay-and-sum beamforming results detailed in this paper, a deconvolution technique (CLEAN, e.g., Sijtsma, 2007) was applied to the microphone array recordings. The aim of such techniques is to reveal weaker acoustic sources that are masked by stronger signals. This is achieved by iteratively removing the array response (including the side lobes) associated with the strongest acoustic source until a stop criterion is reached. In our application this criterion is that no further coherent acoustic power has been removed from the residual measurements during the final iteration. It is assumed that the dominant acoustic source in each iteration can be approximated as a point source, such that a theoretical array response (or point spread function) can be calculated and then removed (see Sijtsma, 2007, for full details of the algorithm). The results are added as an appendix to this paper as they are complementary to the delay-and-sum results. However, a full sensitivity test of the method to variations in input parameters has yet to be completed, such that the results should be considered as preliminary.

The results of the CLEAN algorithm can be represented as source plots (e.g., Fig. B.1).

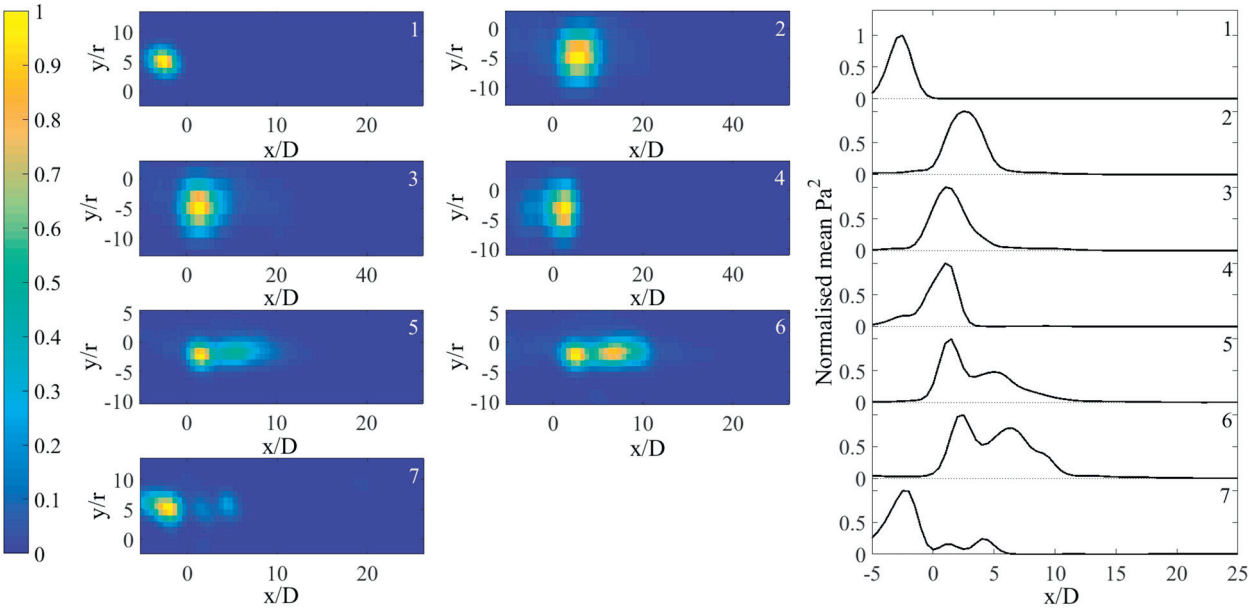

Fig. B.1. Seven example CLEAN source plots. Nozzle geometries, diameters and flow speeds were: 1) Divergent, 0.01 m, 120 m s^{-1}, 2) Convergent, 0.005 m, 97 m s^{-1}, 3) Straight, 0.005 m, 140 m s^{-1}, 4) Straight, 0.005 m, 69 m s^{-1}, 5) Convergent, 0.01 m, 84 m s^{-1}, 6) Convergent, 0.01 m, 98 m s^{-1}, 7) Divergent, 0.01 m, 63 m s^{-1}. Pa^2 values are normalised by the maximum value in each experimental run. Results are the summation over the full 1 to 20 kHz frequency range.

These illustrate the spatial distribution of the sources found iteratively during the CLEAN processing, with the relative amplitudes of the source being represented by the colourscale. The results show that there is good agreement between the axial locations of the peak pressure source estimated using the delay-and-sum beamformer (Fig. 4) and the largest sources found in the CLEAN deconvolution analysis (Fig. B.1). Slight discrepancies for the divergent nozzles, where the CLEAN beamforming estimates exhibit negative axial locations, are not yet fully understood.

Interestingly, the results of the CLEAN algorithm show axially extended sources for the two 0.01 m diameter convergent nozzle cases illustrated in Fig. B.1, compared to the 0.005 m diameter convergent case which exhibits one source with a downstream axial location. This is consistent with the results of the delay-and-sum beamformer, which indicated an upstream peak pressure compared to the axial extent of the potential core. The CLEAN results suggest this may be due to the presence of two spatially separated acoustic sources, with one closer to the nozzle exit. These results highlight the potential of acoustic deconvolution techniques to explore the spatial extent of complex acoustic sources in future studies.

References

Arakeri, V.H., Krothapalli, A., Siddavaram, V., Alkislar, M.B., Lourenco, L.M., 2003. On the use of microjets to suppress turbulence in a Mach 0.9 axisymmetric jet. J. Fluid Mech. 490, 75–98.

Ball, C.G., Fellouah, H., Pollard, A., 2012. The flow field in turbulent round free jets. Prog. Aerosp. Sci. 50, 1–26.

Bogey, C., Barre, S., Bailly, C., 2008. Direct computation of the noise generated from subsonic jets originating from a straight pipe nozzle. Aeroacoustics 7, 1–22.

Bridges, J., Brown, C., 2006. Validation of the Small Hot Jet Acoustic Rig for Jet Noise Research. NASA. (NASA/TM-2006-214234, E-15481).

Caplan-Auerbach, J., McNutt, S., 2003. New insights into the 1999 eruption of the Shishaldin volcano, Alaska based on acoustic data. Bull. Volcanol. 65, 405–417.

Dalton, M.P., White, G.P., Watson, M.I., Nedeau, P.A., 2010. Multiparameter quantification of gas release during weak Strombolian eruptions at Pacaya Volcano, Guatemala. Geophys. Res. Lett. 37, L09303.

Fee, D., Garcés, M.A., Steffke, A., 2010. Characterization of the 2008 Kasatochi and Okmok eruptions using remote infrasound arrays. J. Geophys. Res. 115, D00L10.

Fee, D., Haney, M., Matoza, R., Eaton, A.R.V., Cervelli, P., Schneider, D., Lezzi, A., 2017. Volcanic tremor and plume height hysteresis from Pavlof Volcano, Alaska. Science 355, 45–48.

Fellouah, H., Ball, C., Polard, A., 2009. Reynolds number effects within the development region of a turbulent round free jet. Int. J. Heat Mass Transf. 52, 3943–3954.

Ferdman, E., Otugen, M., Kim, S., 2000. Effect of initial velocity profile on the development of the round jet. J. Propuls. Power 16, 676–686.

Gaeta, R.J., Ahuja, K.K., 2003. Subtle Differences in Jet-noise Scaling with Narrowband Spectra Compared to 1/3 -Otave Band. (AIAA 2003-3124).
Garcés, M., 2013. On Infrasound Standards, Part 1: Time, Frequency, and Energy Scaling. InfraMatics, pp. 13–35
Gee, K., Neilsen, T., Wall, A., Downing, M., James, M., 2013. The sound of freedom: characterizing jet noise from high performance military aircraft. Acoust. Today, pp. 8–21. (July).
Grandchamp, X., Hirtum, A., 2013. Near field round jet flow downstream from an abrupt contraction nozzle with tube extension. Flow Turbul. Combust. 119, 90–95.
Hussein, H., Capp, S., George, W., 1994. Velocity measurements in a high Reynolds-number, momentum-conserving, axisymmetric, turbulent jet. J. Fluid Mech. 258, 31–75.
Johnson, J., Aster, R., Jones, K.R., Kyle, P., McIntosh, B., 2008. Acoustic source characterization of impulsive Strombolian eruptions from the Mount Erubus lava lake. J. Volcanol. Geotherm. Res. 177, 673–686.
Kuttruff, H., 2007. Acoustics. An Introduction. Taylor and Francis, Oxon.
Lau, J.C., Morris, P., Fisher, M., 1979. Measurements in subsonic and supersonic free jets using a laser velocimeter. J. Fluid Mech. 93, 1–37.
Matoza, R., Fee, D., Garcés, M., Seiner, M., Ramon, P., Hedlin, M., 2009. Infrasonic jet noise from volcanic eruptions. Geophys. Res. Lett. 36, 813–822.
Matoza, R., Fee, D., Neilsen, T., Gee, K., Ogden, D., 2013. Aeroacoustics of volcanic jets: acoustic power estimation and jet velocity dependence. J. Geophys. Res. 118, 6269–6284.
McNutt, S.R., Nishimura, T., 2008. Volcanic tremor during eruptions: temporal characteristics, scaling and constraints on conduit size and processes. J. Volcanol. Geotherm. Res. 178, 10–18.
Mi, J., Nobes, D., Nathan, G., 2001. Influence of jet exit conditions on the passive scalar field of an axisymmetric free jet. J. Fluid Mech. 432, 91–125.
Ogden, D., 2011. Fluid dynamics in explosive volcanic vents and craters. Earth Planet. Sci. Lett. 312, 401–410.
Ogden, D., Wohletz, K., Glatzmaier, G., Brodsky, E., 2008. Numerical simulations of volcanic jets: importance of vent overpressure. J. Geophys. Res. 113, B02204.
Olson, J.V., Szuberla, C.A.L., 2008. Processing infrasonic array data signals. In: Havelock, D., Kuwano, S., Vorlander, M. (Eds.), Handbook of signal Processing in Acoustics. vol. 2. Springer, New York, pp. 1487–1496.
Palacios, P.B., Díez, M., Kendall, J.M., Mader, H.M., 2016. Seismic-acoustic energy partitioning during a paroxysmal eruptive phase of Tungurahua volcano, Ecuador. Geophys. J. Int. 205, 1900–1915.
Panchapakesan, N., Lumley, J., 1993. Turbulence measurements in axisymmetric jets of air and helium. Part 1. Air jet. J. Fluid Mech. 246, 197.
Papamoschou, D., 2011. Imaging of directional distributed noise sources. J. Sound Vib. 330, 2265–2280.
Parfitt, E., Wilson, L., 2008. Fundamentals of Physical Volcanology. Blackwell, Oxford.
Polacci, M., Papale, P., Seppia, D., Giordano, D., Romano, C., 2004. Dynamics of magma ascent and fragmentation in trachytic versus rhyolitic eruptions. J. Volcanol. Geotherm. Res. 131, 93–108.
Powell, A., 1953. On the mechanism of choked jet noise. Proc. Phys. Soc. Sect. B 66, 1039.
Quinn, W., 2006. Upstream nozzle shaping effects on near field flow in round turbulent jets. Eur. J. Mech. B. Fluids 25, 279–301.
Rajaratnam, N., 1976. Developments in Water Science. Turbulent Jets. Elsevier, Amsterdam.
Raman, G., Rice, E., Reshotko, E., 1994. Mode spectra of natural disturbances in a circular jet and the effect of acoustic forcing. Exp. Fluids 17, 415–426.
Ripepe, M., Bonadonna, C., Folch, A., Donne, D.D., Lacanna, G., Marchetti, E., Höskuldsson, A., 2013. Ash-plume dynamics and eruption source parameters by infrasound and thermal imagery: the 2010 Eyjafjallajökull eruption. Earth Planet. Sci. Lett. 366, 112–121.
Rossing, T., 1990. The Science of Sound. Second edition, Addison-Wesley, USA.
Rowell, C., Fee, D., Szuberla, C., Arnoult, K., Matoza, R., Firstov, P., Kim, K., Makhmudov, E., 2014. Three-dimensional volcano-acoustic source localization at Karymsky Volcano, Kamchatka, Russia. J. Volcanol. Geotherm. Res. 283, 101–115.
Sijtsma, P., 2007. CLEAN Based on Spatial Source Coherence. (AIAA 2007-3436).
Solovitz, S., Ogden, D., Kim, D., Kim, S.Y., 2014. Coupled fluid and solid evolution in analogue volcanic vents. J. Geophys. Res. Solid Earth 119.
Taddeucci, J., Sesterhenn, J., Scarlato, P., Stampka, K., Bello, E., Fernandez, J., Gaudin, D., 2014. High-speed imaging, acoustic features, and aeroacoustic computations of jet noise from Strombolian (and Vulcanian) explosions. Geophys. Res. Lett. 41, 3096–3102.
Tam, C.K.W., Golebiowski, M., Seiner, J.M., 1996. On the Two Components of Turbulent Mixing Noise from Supersonic Jets. (AIAA 96-1716).
Valentine, G., Wohletz, K., 1989. Numerical models of Plinian eruption columns and pyroclastic flows. J. Geophys. Res. 94, 1867–1887.
Valentine, G., Wohletz, K., 2012. Numerical models of Plinian eruption columns and pyroclastic flows. J. Geophys. Res. 94, 1867–1887.
Vergniolle, S., Caplan-Auerbach, L., 2006. Basaltic thermals and Subplinian plumes: constraints from acoustic measurements at Shishaldin volcano, Alaska. Bull. Volcanol. 68, 611–630.
Viswanathan, K., 2003. Jet aeroacoustic testing: issues and implications. AIAA J. 41, 1674–1689.
Viswanathan, K., 2004. Aeroacoustics of hot jets. J. Fluid Mech. 516, 39–82.
Wang, Y., Devenport, W.J., 2001. Nozzle Applet. (http://www.engapplets.vt.edu - accessed 2014).
Weisgraber, T., Liepmann, D., 1998. Turbulent structure during transition to self similarity in a round jet. Exp. Fluids 24, 210–224.
Wilson, L., Sparks, R., Walker, G., 1980. Explosive volcanic eruptions — IV. The control of magma properties and conduit geometry on eruption column behaviour. Geophys. J. R. Astron. Soc. 63, 117–148.
Wygnanski, I., Fiedler, H., 1969. Some measurements in the self-preserving jet. J. Fluid Mech. 38, 577–612.
Xu, G., Antonia, R.A., 2002. Effect of different initial conditions on a turbulent round free jet. Exp. Fluids 33, 677–683.